文章编号：1001-9014(2025)01-0130-09

DOI:10.11972/j.issn.1001-9014.2025.01.017

Design and validation of RLC equivalent circuit model based on long-wave infrared metamaterial absorber

ZHAO Ji-Cong[1,2], DANG Yan-Meng[1], HOU Hai-Yang[1], LIN Ye-Fan[1], SUN Hai-Yan[1*], ZHANG Kun[2*]

(1. School of Microelectronics and School of Integrated Circuits, Nantong University, Nantong 226019, China;
2. State Key Laboratory of Infrared Physics, Shanghai Institute of Technical Physics, Chinese Academy of Sciences, Shanghai 200083, China)

Abstract: In this paper, we propose an RLC equivalent circuit model theory which can accurately predict the spectral response and resonance characteristics of metamaterial absorption structures, extend its design, and characterize the parameters of the model in detail. By employing this model, we conducted computations to characterize the response wavelength and bandwidth of variously sized metamaterial absorbers. A comparative analysis with Finite Difference Time Domain (FDTD) simulations demonstrated a remarkable level of consistency in the results. The designed absorbers were fabricated using micro-nano fabrication processes, and were experimentally tested to demonstrate absorption rates exceeding 90% at a wavelength of 9.28 μm. The predicted results are then compared with test results. The comparison reveals good consistency in two aspects of the resonance responses, thereby confirming the rationality and accuracy of this model.

Key words: metamaterial, surface plasmons, magnetic dipoles, RLC circuit model

基于长波红外超材料吸收器的RLC等效电路模型设计及验证

赵继聪[1,2], 党岩盟[1], 侯海洋[1], 林叶繁[1], 孙海燕[1*], 张 坤[2*]

(1. 南通大学微电子学院,江苏 南通 226019;
2. 中国科学院上海技术物理研究所 红外科学与技术全国重点实验室,上海 200083)

摘要:提出一种能够准确预测超材料吸收结构光谱响应和共振特性的RLC等效电路模型理论,对其设计进行了扩展,同时详细表征了该模型中的参数。利用该模型,我们对不同尺寸超材料吸波材料的响应波长和带宽进行了计算。与有限差分时域(FDTD)模拟结果相比较,结果吻合很好。所设计的吸收器采用微纳制造工艺制备,通过实验测试,在波长为9.28 μm时,吸收率超过90%。我们将预测结果与测试结果进行对比,表明两者的共振响应具有较好的一致性,从而证实了该模型的合理性和准确性。

关 键 词:超材料;表面等离子体;磁偶极子;RLC电路模型

中图分类号:TN213;TN214　　**文献标识码**:A

Introduction

Infrared detection technology involves multiple disciplines and fields. The uncooled infrared detectors have been used in infrared thermal imaging, energy harvesting, and heat emitters by virtue of their low cost, low power consumption, and small size[1-6]. Among principles inducing electric signals in various types of infrared detectors, the thermoelectric effect is very widely used for especially uncooled infrared detection[7-10]. By absorbing the radiation energy of the target object through infrared-sensitive materials, the energy is converted into heat. With the change in thermal energy, the physical properties of the sensitive element undergo alterations, ultimately transforming this change into an electrical signal to achieve the detection and measurement of the tar-

Received date: 2024-05-04, **revised date**: 2024-06-04　　**收稿日期**:2024-05-04,**修回日期**:2024-06-04

Foundation items: Supported by the National Natural Science Foundation of China (62174092), the Open Fund of State Key Laboratory of Infrared Physics (SITP-NLIST-ZD-2023-04), and the Strategic Priority Research Program of the Chinese Academy of Sciences (XDB0580000).

Biography: ZHAO Ji-Cong (1989-), male, NanTong, master. Research area involves MEMS resonator. E-mail: jczhao@ntu.edu.cn.

* **Corresponding author**: E-mail: sun.yan@ntu.edu.cn; zhangkun@mail.sitp.ac.cn

get object.

In recent years, the emergence of metamaterials has attracted a great deal of attention. Metamaterials are artificially produced composite materials with unique electromagnetic properties not found in nature. The fundamental unit is composed of subwavelength dimensions. By altering the structural dimensions, shape, and spatial arrangement of individual subwavelength basic units, control over the overall or local optical field is achieved at the subwavelength scale. Additionally, it is possible to regulate the dielectric constant and magnetic permeability of composite structures, endowing them with characteristics of nearly perfect absorption in specific frequency bands. This particular electromagnetic property has excellent potential in various applications, including metamaterial absorbers (MAs), photonic crystals, plasmonic resonance, skin effect enhancement, stealth technology, etc[11-13]. The metamaterial absorbers are particularly noteworthy. By integrating the metamaterial absorbers with uncooled infrared detectors, a novel uncooled infrared detection technology is formed. This technology significantly enhances device performance, improves absorption efficiency, and concurrently possesses multispectral detection capabilities.

The most common structure of MAs consists of metal-insulator-metal with a thickness of only subwavelength dimensions. This structure leverages surface plasmons (SPs) at subwavelength scales to achieve strong light-matter interactions. Simultaneously, it realizes ideal absorption responses by reducing reflection and eliminating transmission. In 2008, Landy et al. proposed MAs in microwave band for the first time and achieved greater than 88% absorption at 11.5 GHz by experiments[14]; Hao et al., Liu et al., and Ma et al. used different material stacks and different sub-wavelength size structures to achieve perfect absorption in the short-wave (NIR) and mid-wave (MWIR) infrared window ranges, respectively[15-17]. Currently, there is limited research on metamaterial absorbers in the long-wave infrared (LWIR) spectrum. The existing studies predominantly employ numerical simulation methods, such as Finite Element Method (FEM) and Finite Difference Time Domain (FDTD), for grid partitioning and iterative computations of structural models. As research progresses, various methods have been proposed to predict the resonance mode mechanism of metamaterial absorbers. These methods include transmission line theory, coupling theory, and interference theory[18-22]. The predictions from these theoretical approaches align with simulations and experiments for specific structures. However, compared to previous theoretical methods, there is still a lack of a more convenient and efficient equivalent model approach that can comprehensively and systematically analyze and predict the fundamental principles and resonance responses of MAs structures.

This work introduces long-wavelength infrared window metamaterial absorbers that can be integrated into uncooled infrared detectors. It elucidates the absorption mechanism and resonance principles, followed by design and experimental validation. We simultaneously expanded the RLC equivalent circuit model. By predicting resonance characteristics, including wavelength response and full width at half maximum (FWHM), and comparing them with FDTD simulation results, the rationality of the model was validated. The impact of the structural parameters of the designed MAs on resonance response was analyzed. In the end, we fabricated the MAs by micro-nano fabrication processes and conducted tests using a Fourier Transform Infrared Spectrometer (FTIR). The absorption rate of the sample at 9.28 μm was more than 90%. The test results were compared and validated against the predictions of the RLC circuit, further confirming the feasibility and relevance of the model. This paper comprehensively elucidates the resonant behavior of MAs, providing a profound and intuitive analysis of the resonance response mechanism. The study offers design guidance for the development of efficient and cost-effective novel uncooled infrared detection technologies.

1 Design and simulation

The proposed metal-insulator-metal (MIM) three-layer MAs structure is shown in Fig. 1(a). The structure consists of a 2D periodic array of square-shaped gold (Au) nanostructures on the top, separated by an aluminum nitride (AlN) dielectric layer in the middle and a molybdenum (Mo) metal plate layer at the bottom. The lateral dimensions are width (w) and period (p). The MAs structural chosen parameters in the simulation are shown in Table 1.

Table 1 The structural parameters of the designed MAs
表1 所设计MAs的结构参数

Period	p[μm]	3.6
Characteristic length (width)	w[μm]	2.6
Thickness of top metallic pattern	t_{Au}[nm]	50
Thickness of dielectric spacer	t_{AlN}[nm]	200
Thickness of bottom metallic pattern	t_{Mo}[nm]	100

When a specific infrared light irradiation to the nanometer metal surface, the incident light (surface electromagnetic wave) and the top layer of metal in the free electron element interact to form surface plasmons (SPs), the occurrence of surface plasmon resonance (SPR). This phenomenon induces an electric dipole resonance, which excites the coupling effect between the underlying metal plates through the subwavelength dielectric layer gap, generating a reverse oscillating current and exciting a magnetic dipole. These electric and magnetic dipoles resonate synergistically, effectively dissipating the incident light and achieving high absorption in the target spectral range.

According to the law of conservation of energy, the MAs absorptivity formula is A=1-R-T, where A, R, and T are absorptivity, reflectivity, and transmittance, respectively. When the thickness of the underlying metal Mo is greater than the skinning depth of the LWIR window, the light cannot penetrate, and the transmittance T

is approximated to be 0. Therefore, its absorptivity is A= 1-R. The designed MAs is simulated and analyzed using FDTD software. In the simulation, the light source propagates as a plane wave along the z-axis direction with perfectly matched layer (PML) boundary conditions and periodic boundary conditions along the x and y directions. The dielectric constant and refractive index parameters of the Au material are taken from the literature data of Palik[23]. The material parameters of AlN and Mo are taken from Beliaev and Kirillova[24-25], respectively, and the optical parameters of the simulated bands are shown in Fig. 1(b).

Due to the central symmetry of the designed top nanostructures, the wavelength responses obtained are the same when both transverse magnetic (TM) and transverse electric (TE) waves are used for incidence. In the simulation, the absorption spectrum response is obtained using transverse magnetic (TM) wave incidence, as shown in Fig. 1(c). It is observed in the figure that the absorption peak with nearly 100% absorption at 9.62 μm and T is 0 within the LWIR spectral window.

In order to explore and clarify the mechanism of perfect absorption of MAs in more depth, the electric and magnetic field distributions of the designed MAs at 9.62 μm were computationally characterized and analyzed, as shown in Fig. 2. At the resonance absorption peak, the electromagnetic wave incidence excites the localized surface plasmon electric dipole to couple with the metal film. Localized surface plasmon resonance (LSPR) occurs when the incident light frequency matches the resonance frequency of free electron vibrations. This phenomenon confines the electric field to the interface edge between the top metal and the dielectric region, extending into the dielectric layer, as shown in Fig. 2(a) and (b). Additionally, from the magnetic field distribution characterized in Fig. 2(c) and (d), it can be observed that at a wavelength of 9.62 μm, the electric field vectors interact, causing the motion of free electrons. This interaction leads to oscillating current loops between the two metal interfaces, exciting magnetic dipole resonance. The magnetic moment generated by the oscillating current interacts with the magnetic field of the incident electromagnetic wave, confining the magnetic field within the dielectric layer.

The distribution of the electromagnetic field indicates the combination of localized surface plasmon resonance modes and dipole resonance modes, satisfying the wave vector matching condition of the incident electromagnetic wave. The energy of the incident electromagnetic wave can be effectively confined within the intermediate dielectric layer, as shown in Fig. 2(e) and (f). The coupled electromagnetic energy is converted into thermal energy through the ohmic losses in the bottom metal, achieving perfect absorption.

2 Equivalent model build and analysis

2.1 RLC circuit model

Based on the MAs absorption mechanism, we em-

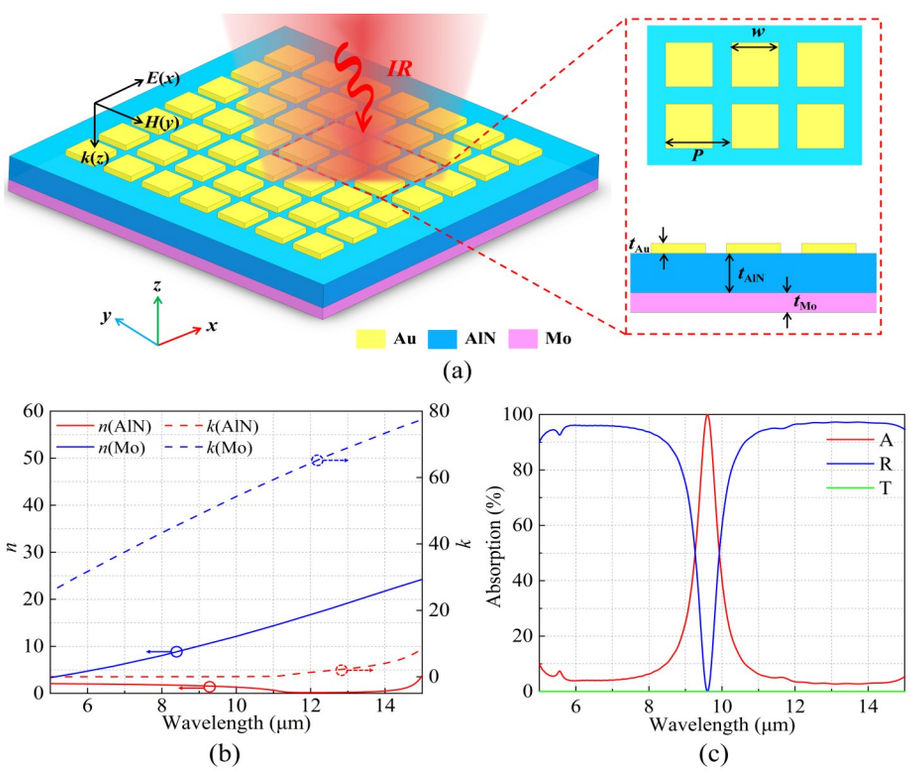

Fig. 1 MIM-MAs infrastructure and related performance: (a) Schematic of the proposed structure of MIM-MAs; (b) Optical parameters of AlN and Mo; (c) Design the schematic diagram of the absorption, reflectivity and transmittance curves of the MAs structure

图1 MIM-MAs基础结构和相关性能:(a) 所提出MIM-MAs结构示意图;(b) AlN和Mo材料的光学参数;(c) MAs结构的吸收、反射和透射响应示意图

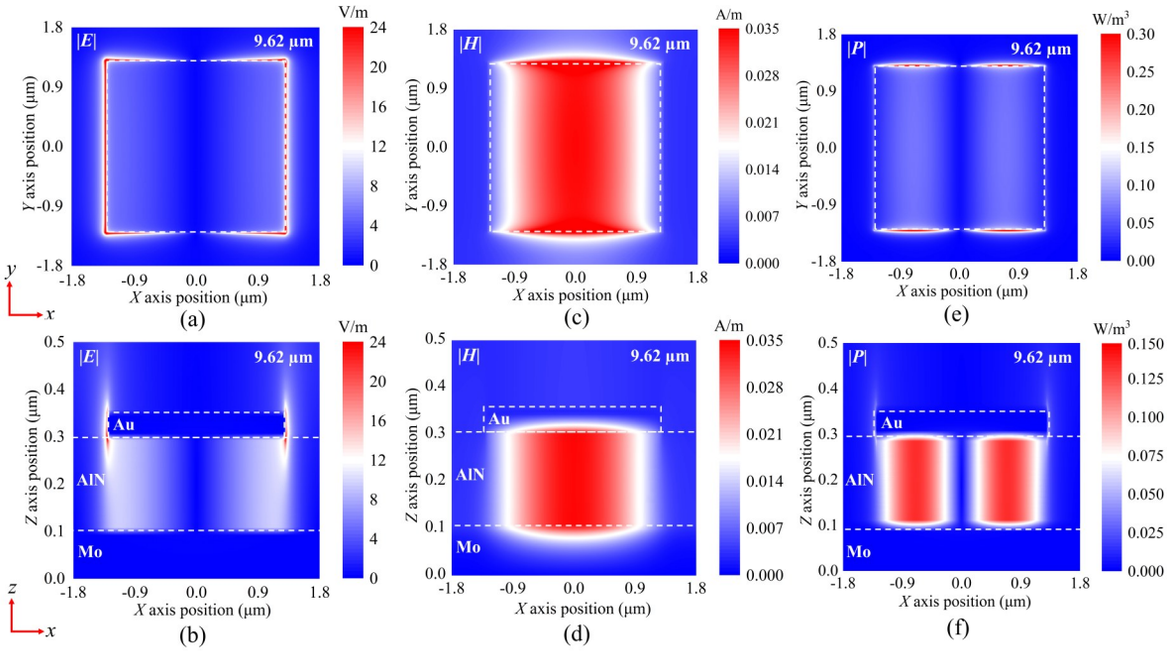

Fig. 2 Mapping of electric and magnetic field distribution at MAs absorption peak: (a) x-y plane and (b) x-z plane electric field distribution; (c) x-y plane and (d) x-z plane magnetic field distribution; (e) x-y plane and (f) x-z plane power density distribution
图2 MAs吸收响应处的电场和磁场分布图:(a) x-y平面和(b) x-z平面电场分布;(c) x-y平面和(d) x-z平面磁场分布;(e) x-y平面和(f) x-z平面功率密度分布

ploy an RLC equivalent circuit model to elucidate the physical mechanisms and resonance effects related to the excitation of localized surface plasmon resonance and magnetic dipole resonance. A. Sakurai et al and J. Zhou et al have developed equivalent circuit models for characterizing the geometric effects of MAs[26-27]. However, for computational efficiency, the former did not account for the dipole interactions between adjacent Au nano units. Similarly, the latter simplified the model by omitting resistive components that cause losses. The electrical characteristics of MAs can be modeled and analyzed more accurately and in detail using the RLC equivalent circuit model, which contributes to a better understanding and optimization of MAs. In addition, this model is not limited to a specific frequency or wavelength range, making it more flexible.

Underneath each subwavelength metal nanostructure exists an independent magnetic field distribution, and these distributions are mutually independent. It can be assumed that the entire device is connected by an equivalent circuit composed of multiple RLC lumped elements. The RLC equivalent circuit model of the extended single subwavelength cell is shown in Fig. 3(a), where the arrows indicate the direction of current flow. The near-field coupling between adjacent subwavelength square gold nanostructures on the top can be approximated as the gap capacitance C_g between two surfaces with non-uniform charge distributions. Similarly, the subwavelength metal nanostructures on the dielectric layer and the metal plate below can be approximated as parallel plate capacitance C_m. Both of these can be derived from the following equations:

$$C_g = \frac{2\pi\varepsilon_0 w}{In\left(\frac{P-w}{t_{Au}}\right)}, \tag{1}$$

$$C_m = \frac{\alpha\varepsilon_0\varepsilon_d w^2}{t_{AlN}}, \tag{2}$$

Where ε_0 ($\approx$8.854×10^{-12} F/m) is the relative permittivity of free space, and ε_d is the relative dielectric constant of the dielectric layer aluminum nitride. In the equation, α ($\approx$ 0.3-0.5) is introduced as a modified tuning factor to consider the non-uniform charge distribution along the metal surface and edge effects[28]. When magnetic dipole resonance occurs, the mutual inductance between the metal layers above and below the dielectric layer can be equivalent to inductance[29-30]:

$$L_m = \frac{\mu_0 t_{AlN}}{2}, \tag{3}$$

Where μ_0 (=4π×10^{-7} H/m) is the vacuum permeability. Within the skin depth range of the metal layer, considering the resistance that induces ohmic and dielectric losses, as well as the dynamic inductance equivalent to the aggregation and oscillation drift of electrons. The distribution of these effects depends on the material and geometric parameters of the top and bottom metals. Therefore, it is necessary to differentiate between the equivalent resistance and dynamic inductance of the upper and lower nano-metal structures. Deriving the dynamic inductance using the conventional inductance formula may not provide a clear representation, and an alternative approach is needed to obtain an equivalent result from a different perspective.

Due to the interaction of electric field vectors, the

current loop at the metal interface is excited, resulting in the resonance of magnetic dipoles. Assuming negligible influence from other factors, all the work done by the current is entirely converted into magnetic field energy. Taking a single MAs structure as an example, the magnetic flux ψ and the increase in magnetic energy dW_m for an RLC circuit can be described as follows:

$$\psi = M_{11} i \,, \tag{4}$$

$$dW_m = i M_{11} di \,, \tag{5}$$

Assuming the current in the circuit starts from zero and increases loop simultaneously rises from zero by the same percentage γ, i. e., $di=Id\gamma$. Through integration, the magnetic field energy Wm converted by the work done by the current loop in a single RLC equivalent circuit can be derived from the following equation:

$$W_m = M_{11} I^2 \int_0^1 \gamma d\gamma = \frac{1}{2} L_1 I^2 \,, \tag{6}$$

Where ψ is the magnetic flux (or magnetic linkage) passing through the circuit, and M_{11} is the mutual inductance coefficient. When only one circuit exists, M_{11} is equal to L_1, representing the inductance within a single current loop. The relationship between the total mass M_e of the moving charges, the drift velocity v when free electrons drift, and the kinetic energy generated by the internal electrons in the metal can be described as follows:

$$M_e = n m_e \delta_m w w' \,, \tag{7}$$

$$v = \frac{I}{new\delta_m} \,, \tag{8}$$

$$W_{ke} = \frac{1}{2} M_e v^2 \,, \tag{9}$$

As shown in equations 10 and 11, δ_m is the skin depth of the metal, and ω_p is the plasma frequency. Where M_e is the mass of a single electron, n is the density, e stands for the charge, and λ and κ are the wavelength and extinction coefficient in free space. During the actual motion, the current distribution of the square gold nanostructures in the top region of the MAs is non-uniform due to edge effects. To accurately calculate the total charge mass, the appropriate size w' should be employed.

$$\delta_m = \frac{\lambda}{2\pi\kappa_m} \,, \tag{10}$$

$$\omega_p^2 = \frac{ne}{m_e \varepsilon_0} \,, \tag{11}$$

Therefore, by energy conservation, the kinetic energy generated by the motion of electrons is equal to the magnetic field energy converted by the work done by the current, i. e., equation 6 is equivalent to equation 9. The final expression for the dynamic inductance is obtained, considering the tuning factor β ($\approx$ 0. 6-0. 8), as shown in equations 12 and 13. The resistance characterizing the losses can be expressed by equations 14 and 15, where ρ_{Au} and ρ_{Mo} are the resistivities of gold and molybdenum, respectively, with parameters obtained from J M Camacho and Yuji Asada[31-32].

$$L_e = \frac{\beta w'}{w\varepsilon_0 \delta_{Au} \omega_p^2} \,, \tag{12}$$

$$L_e' = \frac{w'}{w\varepsilon_0 \delta_{Mo} \omega_p^2} \,, \tag{13}$$

$$R_c = \frac{\beta w' \rho_{Au}}{w\delta_{Au}} \,, \tag{14}$$

$$R_g = \frac{w' \rho_{Mo}}{w\delta_{Mo}} \,, \tag{15}$$

The above RLC lumped circuit elements are all represented using fundamental equivalent formulas for the geometric parameters and material properties of MAs structures. This approach plays an important role in guiding the design and optimization of MAs. Simultaneously, the structure model and physical mechanism of MAs can be reverse-designed and analyzed through backward deduction and iterative computations. The relative impedance $Z_{ri}(\omega)$ and the reflection coefficient $R(\omega)$ of the equivalent circuit model can be described as[33-34]:

$$Z_{ri}(\omega) = \frac{Z_t(\omega)}{Z_0} \,, \tag{16}$$

$$R(\omega) = \left| \frac{Z_t(\omega) - Z_0}{Z_t(\omega) + Z_0} \right|^2 \,, \tag{17}$$

Where $Z_t(\omega)$ and Z_0 are the total set element impedance and free space impedance, respectively. As shown in Fig. 3(b), the simulation calculation by ADS circuit simulation software shows that at the peak wavelength λ_{peak} (= 9. 62 μm) of the MAs absorptivity, the relative impedance $Z_{ri}(\omega)$=1. 019+j0. 033, in which $Re(Z_{ri})\approx1$ and $Im(Z_{ri})\approx0$, i. e., $Z_t(\omega)\approx Z_0$. Under the resonant condition, the reflection $R_{min}(\omega)$ of MAs the incident electromagnetic wave reaches the the minimum, and the absorption $A_{max}(\omega)$ reaches the maximized.

2. 2 Analysis and comparison of predicted parameters

To further substantiate the accuracy of the RLC equivalent circuit model, we calculated resonance conditions for different top subwavelength metal nanostructure widths and periods within this model. The relevant parameters of its associated R, L, and C components have been included in Table 2. Keeping other geometric parameters constant, we compared the predicted resonance results with those obtained using FDTD, as illustrated in Fig. 4.

Fig. 4(a) represents the variation of the peak absorption response wavelength of MAs with w in the range of 2. 2 μm to 3. 2 μm when p=3. 6 μm. It is evident that an increase in w results in a redshift in the peak absorption response wavelength. This can be attributed to the reduced distance between individual unit metal nanostructures, which reduces the restoring force of each unit metal nanostructure, consequently decreasing the resonance frequency. Consequently, the incident light frequency under resonance conditions decreases, leading to a redshift in the response wavelength. When w=2. 6 μm, an increase in p leads to a blueshift in the peak absorption response wavelength, as demonstrated in Fig. 4

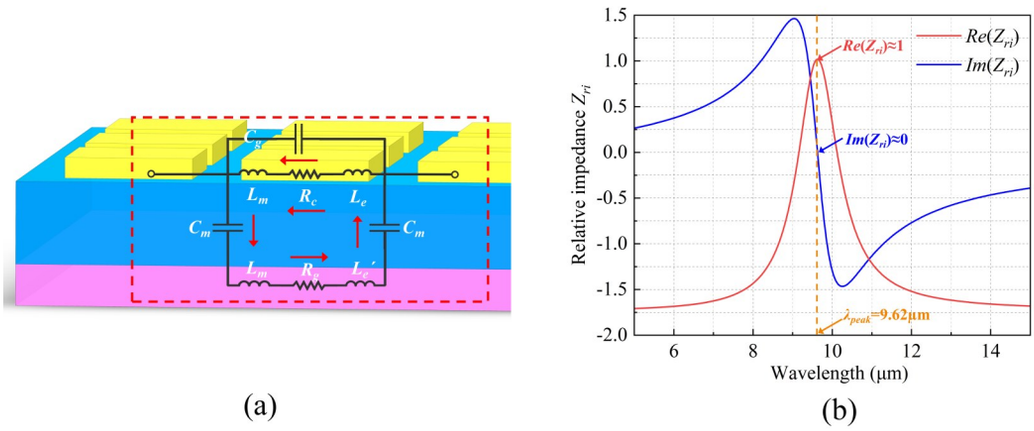

Fig. 3 The proposed equivalent circuit model structure: (a) Schematic diagram of the RLC equivalent circuit model for MIM-MAs; (b) Real and imaginary parts of the relative impedance of the equivalent circuit model
图3 等效电路模型结构:(a) MIM-MAs结构等效电路模型示意图;(b) 等效电路模型相对阻抗的实部和虚部

Table 2 Physical parameters of the RLC circuit model
表2 RLC电路模型的物理参数

w (μm)	λ_{FDTD} (μm)	λ_{RLC} (μm)	C_m (F)	C_g (F)	L_m (H)	L_e (H)	L_e' (H)	R_c (Ω)	R_g (Ω)
2.2	8.97	8.91	1.25×10^{-15}	4.62×10^{-17}	1.26×10^{-13}	6.43×10^{-13}	1.22×10^{-12}	0.45	1.23
2.3	9.16	9.17	1.48×10^{-15}	4.74×10^{-17}	1.26×10^{-13}	6.65×10^{-13}	1.18×10^{-12}	0.43	1.20
2.4	9.32	9.27	1.84×10^{-15}	4.84×10^{-17}	1.26×10^{-13}	6.98×10^{-13}	1.16×10^{-12}	0.34	1.13
2.5	9.46	9.43	2.04×10^{-15}	5.02×10^{-17}	1.26×10^{-13}	7.12×10^{-13}	1.12×10^{-12}	0.38	1.21
2.6	9.63	9.61	2.21×10^{-15}	5.19×10^{-17}	1.26×10^{-13}	7.38×10^{-13}	1.08×10^{-12}	0.41	1.26
2.7	9.75	9.76	2.33×10^{-15}	5.52×10^{-17}	1.26×10^{-13}	7.54×10^{-13}	1.01×10^{-12}	0.41	1.13
2.8	9.87	9.89	2.48×10^{-15}	5.71×10^{-17}	1.26×10^{-13}	7.63×10^{-13}	0.96×10^{-12}	0.40	1.12
2.9	9.99	10.04	2.73×10^{-15}	6.11×10^{-17}	1.26×10^{-13}	7.92×10^{-13}	0.84×10^{-12}	0.39	1.10
3.0	10.09	10.17	2.88×10^{-15}	6.36×10^{-17}	1.26×10^{-13}	8.18×10^{-13}	0.78×10^{-12}	0.39	1.09
3.1	10.20	10.29	3.03×10^{-15}	6.77×10^{-17}	1.26×10^{-13}	8.67×10^{-13}	0.69×10^{-12}	0.40	1.08
3.2	10.31	10.37	3.36×10^{-15}	6.69×10^{-17}	1.26×10^{-13}	8.96×10^{-13}	0.65×10^{-12}	0.38	1.07

(b). The shift in the response wavelength is attributed to the same factors mentioned earlier. The increase in p results in an expanded distance between the metal nanostructures and an increase in the resonance frequency, consequently causing a blueshift in the response wavelength. The results of the response wavelength predicted by the RLC equivalent circuit model better agree with the FDTD simulation results.

Calculations and comparisons were conducted for the FWHM in the absorption response, as shown in Fig. 4(c) and (d). When p=3.6 μm, its FWHM slightly increases as w increases. When w=2.6 μm, its FWHM slightly decreases as p increases. Both phenomena can be attributed to variations in the distance between adjacent metal nanostructures. This alteration makes the coupling effect between them increase or decrease, resulting in a corresponding change in the FWHM. The predicted FWHM is also in better agreement with the FDTD simulation results. Based on the above characterization, the electrical properties and resonance mechanism of the MAs can be analyzed and predicted using the RLC equivalent circuit model. The alignment of this model with the FDTD further substantiates its validity.

3 Fabrication and discussion

Fig. 5(a) shows the fabrication process of the MAs, which is composed of seven main steps: Firstly, a bottom metal Mo with a thickness of 100 nm and an insulator layer AlN with a thickness of 200 nm were successively deposited on the substrate by magnetron sputtering process (step ⅰ) and (step ⅱ); Then, the positive type photoresist is spin coated on the insulator layer AlN and pre-baked, which can make the solvent in the photoresist evaporate quickly and reduces the effect of solvent residue on the pattern (step ⅲ); Next, Ultraviolet (UV) exposure is used to transfer the pattern on the mask to the photoresist (step ⅳ); Developing the photoresist to from the design pattern (step ⅴ); Then, the Au film with a thickness of 50 nm was deposited by magnetron sputtering to form a surface metal layer (step ⅵ); Finally, the lift-off process is realized by using acetone solution to form the designed gold structures (step ⅶ).

The structure comprises a square array of nanostructures, with geometric dimensions outlined in Table 1. Fig. 5(b) depicts the top scanning electron microscope (SEM) image of the fabricated MAs. The performance of the manufactured MAs samples was measured using a

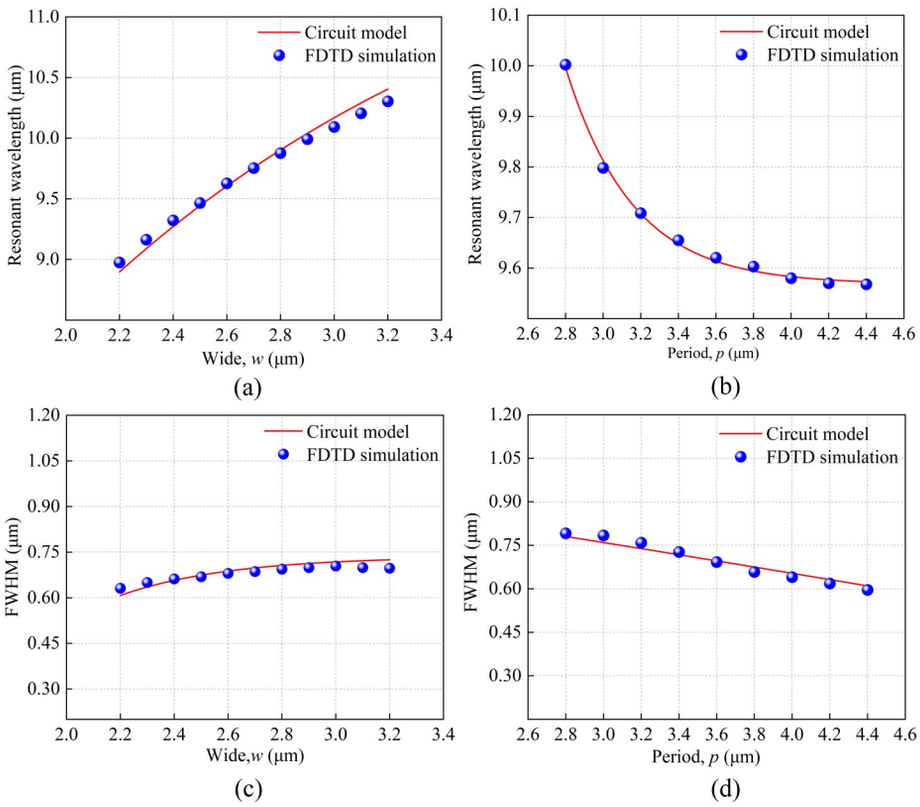

Fig. 4 Comparison of RLC circuit model prediction results and FDTD simulation results: At p=3.6 μm, (a) resonant wavelength and (c) FWHM for different values of w are as follows; At w=2.6 μm, (b) resonant wavelength and (d) FWHM for different values of p are as follows

图4 RLC电路模型预测结果与FDTD仿真结果对比:在p=3.6 μm时不同w值的(a)谐振波长和(c)FWHM;在w=2.6 μm时不同p值的(b)谐振波长和(d)FWHM

Fourier transform infrared spectrometer (Nicolet FTIR 6700). The absorption test results of the MAs samples in the target wavelength range were compared with the predictions of the RLC equivalent circuit model, as shown in Fig. 5(c).

According to the test results, the manufactured MAs samples exhibit an absorption peak at 9.28 μm, where the absorption rate exceeds 90%. The obtained result exhibits slight discrepancies when compared with the predictions from the RLC circuit model. Upon comparing the results, it is evident that the absorption peak in the test results undergoes a blueshift, accompanied by a slight decrease in absorption rate. This phenomenon can be attributed to two terms. First of all, due to insufficient metal surface treatment during the preparation process, some metals are taken away by the photoresist tape during the stripping process, which reduces the width of the square gold nanostructure. Secondly, in terms of material parameters, the optical material constants represented in the circuit model are slightly different from those measured in actual machining. Consequently, this results in deviations in both the wavelength and absorption rate of the absorption peaks.

At wavelengths of 5.94 μm and 11.25 μm, parasitic peaks with absorption rates below 40% are present. This is attributed to the incomplete removal of residual photoresist on the MAs surface during the lift-off process. The residual photoresist adheres to the metal surface, leading to the appearance of local parasitic peaks and exerting a certain influence on the test results. In the subsequent preparation process, the optimization of processing steps and parameters can effectively prevent the occurrence of the aforementioned issues. Overall, the RLC equivalent circuit model provides a good prediction for MAs.

4 Conclusion

In this study, a theoretical model and experimental validation of MIM metamaterial absorbers that can be integrated with an uncooled infrared detector are presented. The RLC equivalent circuit model is extended and designed to explain and analyze the physical mechanism and resonance effect of MAs in depth based on the geometrical effect of the structure. The model successfully predicted the resonant characteristics, including the resonance frequency and FWHM. The designed MAs structures were fabricated using micro-nano processing techniques and subjected to FTIR testing. The results indicate that absorption rates exceeding 90% were achieved at a wavelength of 9.28 μm. Comparing the predicted results of this model with the FDTD simulation calculation results and test results, a better resonance response match is obtained, which further verifies the rationality

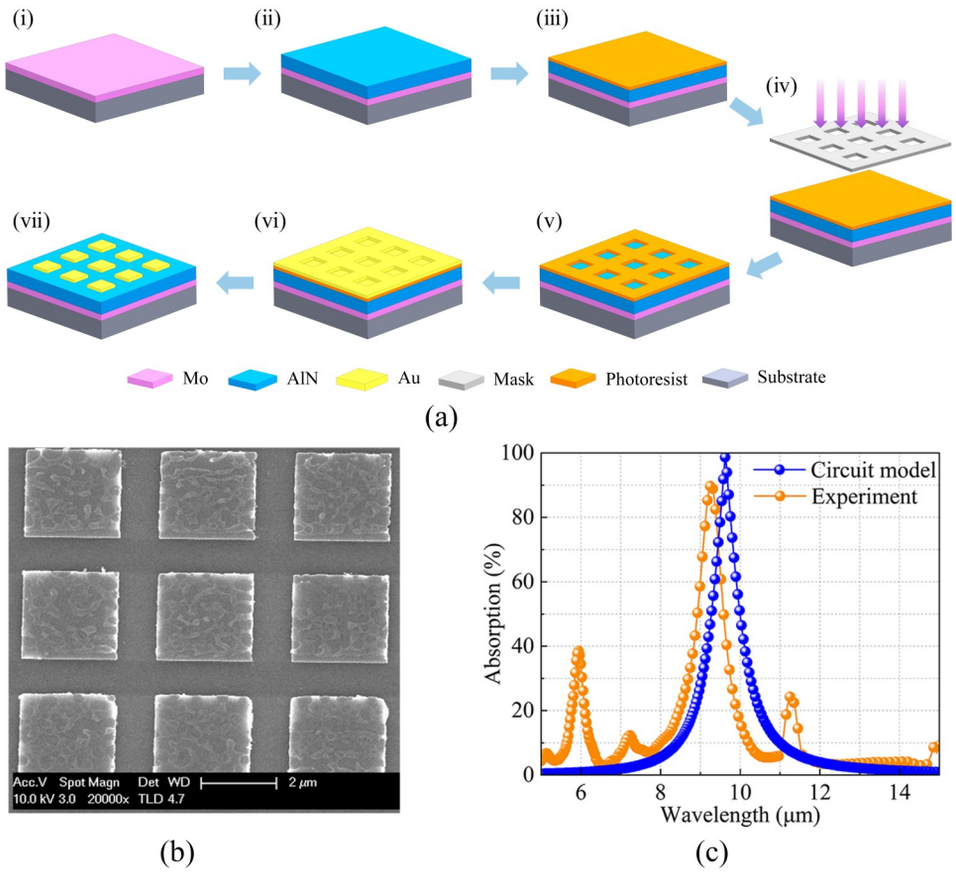

Fig. 5 Preparation by MIM-MAs process: (a) Process steps to fabrication MAs; (b) SEM image of the fabricated MAs; (c) Tested MAs absorption response (orange points) versus the absorption response predicted by the RLC equivalent circuit model (blue points)
图5 MIM-MAs工艺制备:(a) 制备MAs工艺步骤;(b)所制备MAs的SEM图像;(c)测试MAs的吸收响应(橙色)与RLC等效电路模型预测的吸收响应(蓝色)对比

and accuracy of the model. This study contributes to an in-depth understanding of the wavelength response and resonance mechanism of MAs and guides the design and optimization of metamaterial absorbers.

References

[1] Gumin, Kang, Haesung, et al. Broadband Light-Trapping Enhancement in an Ultrathin Film a-Si Absorber Using Whispering Gallery Modes and Guided Wave Modes with Dielectric Surface-Textured Structures[J]. *Advanced Materials*, 2013, **25**(18): 2617-2623.
[2] Wang D L , Su G. New strategy to promote conversion efficiency using high-index nanostructures in thin-film solar cells[J]. *Scientific Reports*, 2014, **4**(1): 7165.
[3] Källhammer J E, Pettersson H, Eriksson D, *et al*. Fulfilling the pedestrian protection directive using a long-wavelength infrared camera designed to meet both performance and cost targets[C]. Photonics in the Automobile II, SPIE 2006, **6198**: 74-84.
[4] GUO Guang-Hao, WU Nan-Jian, LIU Li-Yuan. Low power application specific SoC chip for uncooled infrared image processing[J]. Journal of Infrared and Millimeter Waves, 2023, **42**(1): 122-131. (郭广浩, 吴南健, 刘力源. 低功耗非制冷红外图像处理专用SoC芯片[J]. **红外与毫米波学报**), 2023, **42**(1):122-131.
[5] SANG Mao-Sheng, XU Guo-Qing, QIAO Hui, *et al*. High speed uncooled MWIR infrared HgCdTe photodetector based on graded bandgap structure[J]. Journal of Infrared and Millimeter Waves, 2022, **41**(6): 972~979.(桑茂盛, 徐国庆, 乔辉, 等. 基于梯度能带结构的高速非制冷中波红外HgCdTe探测器[J]. **红外与毫米波学报**), 2022, **41**(6):972~979.
[6] Wang F, Liu Z, Zhang T, *et al*. Fully Depleted Self-Aligned Heterosandwiched Van Der Waals Photodetectors[J]. *Advanced Materials*, 2022, **34**(39): 2203283.
[7] Wang F, Zhang T, Xie R, *et al*. Next-generation Photodetectors Beyond van der Waals Junctions[J]. *Advanced Materials*, 2024, **36**(3): 2301197.
[8] Chen Y, Wang Y, Wang Z, *et al*. Unipolar barrier photodetectors based on van der Waals heterostructures[J]. *Nature Electronics*, 2021, **4**(5): 357-363.
[9] Hu W, Ye Z, Liao L, *et al*. 128×128 long-wavelength/mid-wavelength two-color HgCdTe infrared focal plane array detector with ultralow spectral cross talk[J]. *Optics Letters*, 2014, **39**(17): 5184-5187.
[10] Hu W D, Chen X S, Ye Z H, *et al*. A hybrid surface passivation on HgCdTe long wave infrared detector with in-situ CdTe deposition and high-density Hydrogen plasma modification[J]. *Applied Physics Letters*, 2011, **99**(9): 091101.
[11] Xie R, Wang P, Wang F, *et al*. Simultaneous control of intensity, phase, and polarization in real time under a weak oscillation theory [J]. *Optics Letters*, 2021, **46**(6): 1361-1364.
[12] Ge H, Xie R, Chen Y, *et al*. Skin effect photon-trapping enhancement in infrared photodiodes[J]. *Optics Express*, 2021, **29**(15): 22823-22837.
[13] Ge H N, Xie R Z, Guo J X, *et al*. Artificial micro-and nano-structure enhanced long and very long-wavelength infrared detectors[J]. *Acta Physica Sinica*, 2022, **71**(11): 110703.
[14] Landy N I, Sajuyigbe S, Mock J J, *et al*. Perfect Metamaterial Absorber[J]. *Physical Review Letters*, 2008, **100**(20): 207402.
[15] Hao J, Wang J, Liu X, *et al*. High performance optical absorber based on a plasmonic metamateria[J]. *Applied Physics Letters*, 2010, **96**(25): 251104.
[16] Liu X, Tyler T, Starr T, *et al*. Taming the Blackbody with Infrared Metamaterials as Selective Thermal Emitters[J]. *Physical Review Letters*, 2011, **107**(4): 045901.

[17] Ma W, Wen Y, Yu X. Theoretical and Experimental Demonstrations of a Dual-Band Metamaterial Absorber at Mid-Infrared [J]. *IEEE Photonics Technology Letters*, 2014, **26**(19): 1940-1943.
[18] Lin Z C, Zhang Y, Li L, *et al*. Extremely wideband metamaterial absorber using spatial lossy transmission lines and resistively loaded high impedance surface [J]. *IEEE Transactions on Microwave Theory and Techniques*, 2023, **71**(8): 3323-3332.
[19] Liang C, Kong X, Wang F, *et al*. A broadband perfect metamaterial absorber with angle-insensitive characteristics [J]. *Journal of Electromagnetic Waves and Applications*, 2023, **37**(3): 401-410.
[20] Zhu L, Sandhu S, Otey C, *et al*. Temporal coupled mode theory for thermal emission from a single thermal emitter supporting either a single mode or an orthogonal set of modes [J]. *Applied Physics Letters*, 2013, **102**(10): 103104.
[21] Wanghuang T, Chen W, Huang Y, *et al*. Analysis of metamaterial absorber in normal and oblique incidence by using interference theory [J]. *Aip Advances*, 2013, **3**(10): 102118.
[22] WU Xiang, PEI Zhi-Bin, QU Shao-Bo, *et al*. Design and experimental verification of band-pass frequency selective surface based on metamaterial effective medium theory [J]. Journal of Infrared and Millimeter Waves, 2011, **30**(5): 469-474.(吴翔, 裴志斌, 屈绍波, 等. 基于超材料等效介质理论的带通频率选择表面设计及验证 [J]. **红外与毫米波学报**), 2011, **30**(5): 469-474.
[23] Palik E. D. Handbook of Optical Constants of Solids [M]. Academic Press, 1997, 3.
[24] Beliaev L Y, Shkondin E, Lavrinenko A V, *et al*. Thickness-dependent optical properties of aluminum nitride films for mid-infrared wavelengths [J]. *Journal of Vacuum Science & Technology A*, 2021, **39**(4): 043408.
[25] KffiiLLOVA M M, Nomerovannaya L V, Noskov M M. Optical Properties of Molybdenum Single Crystals [J]. *Journal of Experimental and Theoretical Physics*, 1971, **33**(6): 2252-2259.
[26] Sakurai A, Zhao B, Zhang Z M. Resonant frequency and bandwidth of metamaterial emitters and absorbers predicted by an RLC circuit model [J]. *Journal of Quantitative Spectroscopy and Radiative Transfer*, 2014, **149**: 33-40.
[27] Lee B J, Wang L P, Zhang Z M. Coherent thermal emission by excitation of magnetic polaritons between periodic strips and a metallic film [J]. *Optics Express*, 2008, **16**(15): 11328-11336.
[28] Zhou J, Economon E N, Koschny T, *et al*. Unifying approach to left-handed material design [J]. *Optics Letters*, 2006, **31**(24): 3620-3622.
[29] Wang L P, Zhang Z M. Phonon-mediated magnetic polaritons in the infrared region [J]. *Optics Express*, 2011, **19**(102): A126-A135.
[30] Lee B J, Wang L P, Zhang Z M. Coherent thermal emission by excitation of magnetic polaritons between periodic strips and a metallic film [J]. *Optics Express*, 2008, **16**(15): 11328-11336.
[31] Camacho J M, Oliva A I. Surface and grain boundary contributions in the electrical resistivity of metallic nanofilms [J]. *Thin Solid Films*, 2006, **515**(4): 1881-1885.
[32] Asada Y. Superconductivity of alloy films of Mo and simple metal elements [J]. *Journal of Applied Physics*, 1985, **58**(8): 3162-3165.
[33] Wang Y, Xuan X, Wu S, *et al*. Reverse design of metamaterial absorbers based on an equivalent circuit [J]. *Physical Chemistry Chemical Physics*, 2022, **24**(34): 20390-20399.
[34] Li F, Issah I, Baah M, *et al*.Polarization-dependent wideband metamaterial absorber for ultraviolet to near-infrared spectral range applications [J]. *Optics Express*, 2022, **30**(15): 25974-25984.